2016

Development of analysis approaches to calcium-imaging data of hippocampal neurons associated with classical conditioning in mice

https://hdl.handle.net/2144/19497

Boston University

BOSTON UNIVERSITY

COLLEGE OF ENGINEERING

Thesis

DEVELOPMENT OF ANALYSIS APPROACHES TO CALCIUM-IMAGING DATA OF HIPPOCAMPAL NEURONS ASSOCIATED WITH CLASSICAL CONDITIONING IN MICE

by

ZHAOJIE YAO

B.Med., Zhejiang University, 2014

Submitted in partial fulfillment of the
requirements for the degree of
Master of Science

2016

Approved by

First Reader

Xue Han, Ph.D.
Assistant Professor of Biomedical Engineering

Assistant Professor of Pharmacology & Experimental Therapeutics
School of Medicine

Second Reader

Nancy Kopell, Ph.D.
Professor of Mathematics & Statistics

Third Reader

Kamal Sen, Ph.D.
Associate Professor of Biomedical Engineering

DEDICATION

I would like to dedicate this work to my supporting family, and my furry friends, Chancellor Bismarck and King Songtsen Gampo.

ACKNOWLEDGMENTS

I would like to thank my advisor and the thesis committee for directing me through the research and composition of this thesis. Their insights and feedbacks are very essential to the accomplishment of this work. I dedicate my sincere thanks my advisor Dr. Xue Han has taught me a dynamic and multi-faceted approach to addressing scientific inquiry, and shown me how to confront the depth and subtlety when interpreting data analysis results.

I would also like to express gratitude for all of the members of my laboratory who offered unconditional advice and technical advice over the past two years. Especially, I am deeply grateful to Dr. Howard Gritton and Dr. Nicholas James who have been great mentors to me.

Finally, I would like to thank my parents for supporting my education and academic pursuit, and my loving pets Bismarck and Gampo who have kept me company during my late-night work.

DEVELOPMENT OF ANALYSIS APPROACHES TO CALCIUM-IMAGING DATA OF HIPPOCAMPAL NEURONS ASSOCIATED WITH CLASSICAL CONDITIONING IN MICE

ZHAOJIE YAO

ABSTRACT

Recent improvements in high performance fluorescent sensors and scientific CMOS cameras enable optical imaging of neural networks at a much larger scale. Our lab has demonstrated the ability of wide-field calcium-imaging (using GCaMP6f) to capture the concurrent dynamic activity from hundreds to thousands of neurons over millimeters of brain tissue in behaving mice. The expansiveness of the neuronal network captured by the system requires innovation in data analysis methods. This thesis explores data analysis techniques to extract dynamics of hippocampal neural network containing a large number of individual neurons recorded using GCaMP6, while mice were learning a classical eye puff conditioning behavior.

GCaMP6 fluorescence signals in each neuron is first considered one dimension, and each dataset thus contains hundreds to thousands dimensions. To understand the network structure, we first performed dimension reduction technique to examine the low-dimension evolution of the neural trajectory using Gaussian Process Factor Analysis, which smooths across dimensions, while extracting the low dimension representation. Because of the slow time course of GCaMP6 signals, the Factor Analysis was biased to the long lasting decay phase of the signal that does not represent neural activities. We found that it is critical to first estimate the spike train inference prior to application of dimension reduction, such as using the Fast Nonnegative Deconvolution method. While the low-dimension presentation described intriguing features in the neural trajectories that paralleled the learning behavior of the animal, to further quantify the network changes we directly examined the network in the high dimension space. We calculated the changes in the distance of the network trajectory over time in the high dimension space without any filtering, and compared across different phases of the behavioral states. We found that the speed of the trajectory in the high dimension space is significantly higher when animal learned the task, and the trajectory travelled much further away from baseline during the delay phase of the conditioning behavior. Together, these results demonstrate that dimension reduction analysis technique and the network trajectory within the non-reduced high dimension space can capture evolving features of neural networks recorded using calcium imaging. While this thesis concerns the hippocampal dynamics during learning, such data analysis techniques are expected to be broadly applicable to other behaviorally relevant networks.

TABLE OF CONTENTS

LIST OF FIGURES

LIST OF ABBREVIATIONS

FRET	Förster resonance energy transfer
GP	Gaussian-process
GPFA	Gaussian process factor analysis
ITI	inter-trial interval
MAP	maximum a posteriori probability
MLE	maximum likelihood estimation
PCA	principal component analysis
ROI	region of interest
SD	standard deviation
SE	square exponential
SEM	standard error of the mean
TIFF	tag image file format
US	unconditioned stimulus

INTRODUCTION

Behavioral neuroscience is the application of the principles of biology to the study of physiological, genetic, and developmental mechanisms of behavior in humans and other animals. The primary levels of research in behavioral neuroscience involve neurons and brain circuitry, in the investigation of which, various techniques, including calcium imaging, have been developed and matured in use. However, corresponding full-fledged data analysis methods are still scarce. Although new methods are being developed on an accelerated rate, most of them have yet to be accepted by a wide range of researchers, largely due to inefficiency in generating straight-forward biological implications.

Lately, multiple development in technology has achieved advance of calcium imaging in neuroscience. In particular, the latest generation of genetically encoded GCaMP6 family of calcium sensors has remarkable sensitivity and has promoted the precision of calcium imaging of neurons to a new level (Sun *et al.*, 2013). On the other hand, the relatively older wide-field, i.e. single photon imaging, is making a come-back, after having been in use for several decades. It offers unique advantages if the main scientific objective is to simultaneously record a large number of neurons in the brain with high temporal fidelity. However, an emerging technical challenge that parallels advances in imaging large brain areas with high spatiotemporal resolution is the processing of correspondingly large datasets.

Previously, our lab has demonstrated the ability of wide-field calcium-imaging (using GCaMP6f) to capture the concurrent dynamic activity from hundreds to thousands of neurons over millimeters of brain tissue in behaving mice. In the meantime, we developed software to facilitate rapid downstream data processing. However, the expansiveness of the neuronal network captured by the system requires innovation in analysis methods.

Dimension Reduction for Large-scale Neural Network Data

Development in our imaging technologies have made possible the recordings of neural activity of networks involving hundreds to thousands of neurons. Simultaneously, it has enabled the study of dynamics of neurons on a population level. Thus, the analysis strategy suitable for neural activity at individual level needs to be updated accordingly in a population framework, where dimension reduction methods display their potential.

Dimensionality reduction methods can fetch low-dimensional representations from the high-dimensional data. The representation is often able to separate or highlight some feature of interest in the data, which might be overwhelmed by noise in the high-dimension space. These methods have begun to shed light into the mechanisms underlying various phenomena, including but not limited to the selection and integration of sensory input during decision-making in prefrontal cortex (Mante *et al.*, 2013), the ability of premotor cortex to prepare movements without executing them (Kaufman *et al.*, 2014), and odor discrimination in the olfactory system (Mazor *et al.*, 2005). Dimensionality reduction has also been fruitfully applied to population recordings in other studies of decision-making (Harvey *et al.*, 2012; Stokes *et al.*, 2013; Briggman *et al.*, 2005), the motor system (Churchland *et al.*, 2010; Churchland *et al.*, 2012; Yu *et al.*, 2009) and the olfactory system (Broome *et al.*, 2006; Saha *et al.*, 2013), as well as in working memory (Rigotti *et al.*, 2013; Machens *et al.*, 2010), visual attention (Cohen *et* *al.*, 2010), the auditory system (Luczak *et al.*, 2009), rule learning (Durstewitz *et al.*, 2010), speech (Bouchard *et al.*, 2013) and more.

Dimensionality reduction methods can render single-trial analysis statistical power (Cunningham *et al.*, 2014). Traditionally, smoothing of neural responses typically requires averaging noisy spiking activity across multiple experimental trials to obtain firing rates that vary smoothly over time. However, if the neural activity is not a direct function of externally measurable or controllable variables (for example, if activity is more a reflection of internal processing than stimulus drive or measurable behavior), the time course of neural responses may differ substantially on nominally identical trials. Using dimension reduction methods, we can leverage statistical power across multiple neurons to extract a succinct summary of the population activity on individual experimental trials.

Dimensionality reduction can also facilitate exploratory data analysis of large-scale neural network (Cunningham *et al.*, 2014). Exploratory data analysis involves the visualization of a large dataset, which can help generate insightful hypotheses. However, because the neurons in the same network often show heterogeneous dynamics, it is rarely possible to simplify all responses in a cohesive unison. Dimensionality reduction, by giving a low dimensional summary of the high-dimensional population activity, makes possible reviewing the population as a whole. This step provides an initial assessment of the salient features of the data while guiding subsequent analyses.

METHODS

Imaging Setup and Animal Experiment

Our lab (Mohammed *et al.*, 2016) customized a conventional epifluorescence microscope for recording in awake head fixed mice. The microscope consists of a 10X objective lens for increased imaging area, a high intensity LED that can be precisely controlled via TTL pulses, a filter set appropriate for imaging GCaMP6 fluorescence, and a scientific CMOS camera capable of imaging large areas at high speed (Fig. 2.1A). Our lab imaged the hippocampal CA1 region, which consists of a thin and densely packed pyramidal cell layer nested between two thick and sparsely populated layers (Fig. 2.1B).

Mice were surgically injected with AAV-synapsin-GCaMP6f virus into the CA1 pyramidal cell layer, and then chronically implanted with an imaging window for optical recording (Fig. 2.1B). The mice were trained on a simple trace conditioning behavioral task that is known to depend on the hippocampus and involve CA1 neurons (Mohammed *et al.*, 2016). In trace conditioning, animals come to associate two stimuli that are otherwise unrelated. In this case, the conditioned stimulus, a 350ms long tone, precedes the unconditioned stimulus, a gentle air puff to one eye, with a 250ms interval (the trace interval) (Fig. 2.1C). Each training session consisted of 40 tone-puff trials with a 31–36 second randomized inter-trial interval (ITI). Performance is quantified via anticipatory eye lid movement that occurs in response to tone, but precedes air puff (Fig. 2.1C).

Fluorescence imaging was performed at 20Hz with an image resolution of 1024x1024 pixels, while an animal was performing trace conditioning training. The camera was coupled to a 10X objective lens and thus each pixel corresponds to

1.312x1.312 μm^2, which yields an imaging field of view of 1.343x1.343 mm^2. Imaging data were acquired at 16 bits/pixel, which results in about 50 GB of imaging data in a typical 25 minutes recording session. Data acquisition was performed with the commercial software package HCImageLive running on a multicore computer to facilitate high speed streaming from the camera to RAM. At the end of a recording session, imaging data was transferred from RAM to the hard drive for long-term storage and processing. Behavioral stimuli and image acquisition were triggered by TTL pulses that were controlled via customized Matlab functions, and recorded for offline validation. Imaging data was stored as multi-page tag image file format (TIFF) and processed offline.

Eyelid position was monitored using Point Grey FlyCapture 2 software and Flea3 USB3.0 camera. Eyelid position was calculated by tracing the area of the eye using ImageJ when it was opened at its maximum. The eye and surrounding area was illuminated using an IR lamp positioned approximately 0.5 meters away. Using this configuration, eye lid area can be recorded as an increase in reflection that occurs as the eyelid closes impinging on the defined eye region.

Correct trials were characterized as those with changes in (first derivative of) reflection that surpassed a significance threshold defined by that trials baseline activity.

The response window consisted of the 600 ms period following CS onset but prior to air-puff delivery, during which the mean absolute value of first derivative of reflection values was calculated. The mean absolute baseline reflection change was sampled from nine 600 ms intervals prior to sound onset, i.e. [n-0.9 n-0.3] s (n=-0, -1…-8) with 0 referring to CS onset. The maximum deviation of the response window from the baseline was characterized as the largest increase of response window mean absolute reflection change compared to the nine baseline intervals.

The threshold of was calculated in a randomization framework. In each iteration, random pairs of 600 ms intervals were collected from reflection change traces other than those that fell within 15 s after the sound. The mean absolute reflection change was calculated between each pair to generate the iteration distribution, and the 90 percentile was extracted to represent each iteration and subsequently forming a distribution. The threshold was the defined as the median of that distribution.

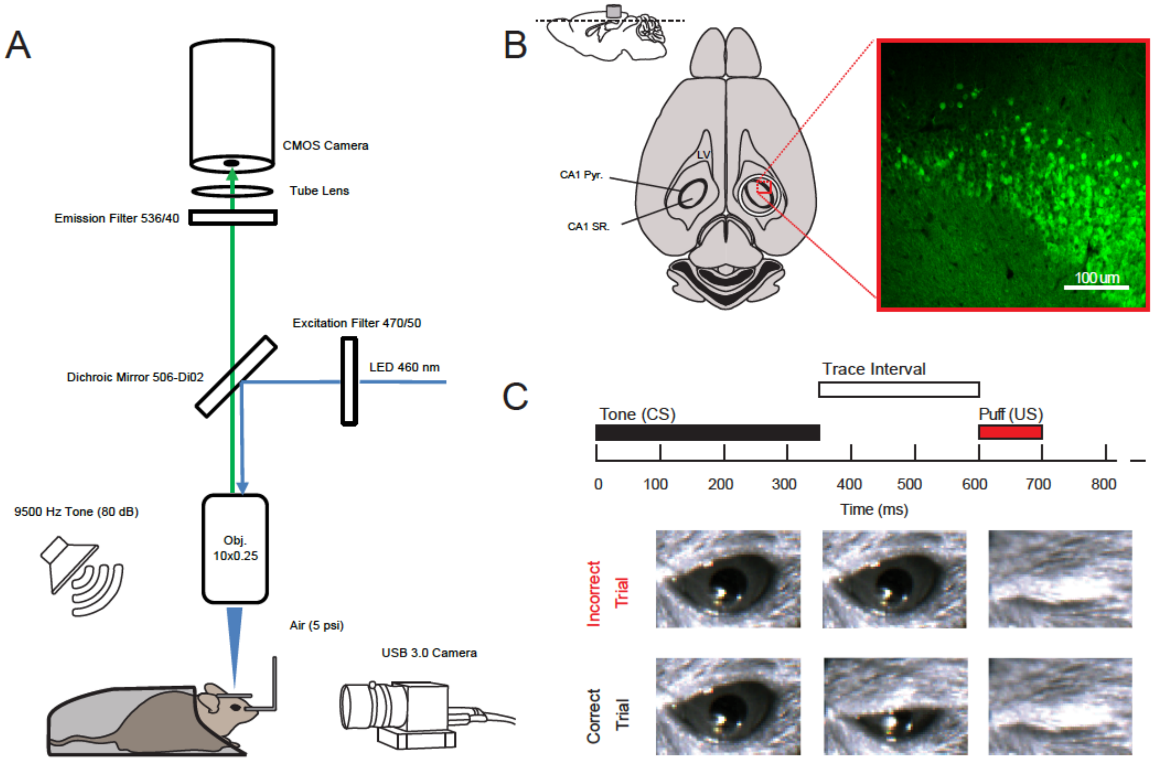

Figure 2.1 Experimental setup and behavioral design (Mohammed *et al.*)**:** (A) Diagram of image acquisition system and behavioral apparatus. Ca2+ signals were captured using a CMOS camera and illumination was achieved using a 460 nm LED. Animals were positioned via a head holder under a 10X objective lens. Air puffs were delivered via a cannula directed at the right eye

and a USB 3.0 camera was used to monitor eyelid position at 20Hz. Auditory cues were delivered at 80dB from a speaker positioned from behind the animal. (B) Anatomical depiction of cannula placement and imaging plane. A representative confocal image from the animal analyzed in figures 2–5. Cannula is to scale: note that dorsal CA1 pyramidal cell layer below the cannula (CA1 pyr: stratum pyramidale; SR, stratum radiatum; LV, lateral ventricle). (C) Trace eyeblink paradigm. A 350 ms duration, 9500 Hz pure tone served as the conditioned stimulus (CS). The CS was followed by a 250 ms trace interval, which was followed by a 5 psi, 100 ms long, air puff to the eye that served as the unconditioned stimulus (US). Eyelid movement displacement was analyzed offline at the conclusion of the recording.

Image Processing

Image processing was performed offline using MATLAB software. The goal of this procedure was to reduce the raw image sequence to a collection of one-dimensional traces, where each trace indicates the fluorescence intensity of an individual neuron over time, and the collection approximates the distinct activity of each and every neuron in the imaging field of view. We implement the process in 3 distinct stages as described below (Mohammed *et al.*, 2016).

Image Pre-processing: Contrast Enhancement and Motion Correction

Alignment of each frame in the image sequence with all other frames is essential to the methods we use in subsequent steps for identifying and tracking pixels over time. Thus, the goal of the first stage is to correct for any misalignment caused by movement of the brain tissue relative to the microscope and camera.

We preceded our main motion correction procedure with a contrast enhancement step that attempts to mitigate the effect of any non-uniform illumination of the brain tissue. Any illumination non-uniformity will be stationary in the camera's field of view despite motion of the illuminated brain, which would hamper motion detection accuracy, or alternatively produce artifacts in accurately motion-corrected frames if left uncorrected. This enhancement is essentially a high-pass filtering operation, however the filtering must be performed in the log domain because of the multiplicative nature of light absorption. Additionally, artifacts often associated with digital high-pass filtering can be mitigated by equivalently computing a low-pass filtered component of each frame, then subtracting the low-pass component from the original image. This log-domain filtering operation is often described as “Homomorphic filtering”.

Many algorithms for estimating and correcting image displacement exist and are well described in the medical imaging literature. We elected to use phase-correlation to estimate the induced motion in each frame, as we found this method to be highly stable, moderately accurate, and most importantly, fast, especially when implemented in the frequency domain and using a quality graphics card.

The operation estimates the mean translational displacement between two frames, one being the template or “fixed” frame, and the other being the uncorrected or “moving” frame. In the spatial domain this is accomplished by computing the normalized cross-correlation, which implies a 2-dimensional convolution of large matrices. The equivalent operation in the frequency domain is a simple scalar dot-product of the discrete Fourier transforms of each image normalized by the square of the template, followed by the inverse Fourier transform. The intermediate result is the cross-correlation (or phase-correlation) matrix, which should have a peak in its center for correctly aligned images, or a peak near the center, the offset of which indicates the mean offset between the two images. This peak can be found with subpixel precision by interpolation to give a more accurate alignment, although at some moderate expense in computation time.

For the template image we used a moving average of previously aligned frames when processing frames sequentially, which was averaged with a fixed mean of randomly sampled and sequentially aligned images from the entire set when processing files in parallel. The simplest way to perform this operation is to use the built-in MATLAB function *normxcorr2*, which makes optimization decisions based on image size and available hardware automatically. However, performance can be improved by tailoring the operation to your particular hardware and image size, i.e. using *fft2* and *ifft2* for large images and a good graphics card.

After aligning sequential image frames, we were able to estimate a baseline value and other statistics for each pixel (maximum, minimum, mean, standard-deviation, etc.), and use these statistics to reduce the bit-depth of frames being passed to the next stage. This was done purely to speed computation in subsequent steps, but won't necessarily be helpful in all cases. For the results presented here, the motion-corrected images were saved as a new video file with 8 bit dynamic range, with the top 1% intensity saturated at 255 and the bottom 1% set at 0.

Region of Interest (ROI) Detection

The ROI detection process used an adaptive threshold on the z-score of pixel intensity to reduce each frame to binary 1′s and 0′s (logical true or false). These binary frames were then processed using morphological operations to find and label connected components within each frame. For example, beginning with a z-score threshold of 1.5, all pixels that were more than 1.5 standard deviations above their mean were reduced to 1 (true), and all others reduced to 0 (false). Pixels reduced to 1 were often pixels overlying a cell that was significantly brighter during that frame due to activation of GCaMP. This initial threshold was adjusted up or down based on the number of non-zero pixels detected with each threshold. This was done to prevent spurious motion-induced shifts of the image frame from producing ROIs along high contrast borders. All morphological operations were performed using built-in MATLAB functions from the Image Processing Toolbox, which have fast parallel versions if the operation is run on a graphics card (e.g. *imclose, imopen*, etc.). Furthermore, the connected-component labeling and region formation operations were run using built-in MATLAB functions *bwconncomp*, and *regionprops*. Connected components were stored in a custom class and termed “single-frame ROIs,” and these were then passed to the 3rd stage of processing, which merges them into a “multi-frame ROI” that represents the location and spatial distribution of each cell identified over the entire video.

ROI Merging

The standard structure of region properties output by the MATLAB function *regionprops* (Area, BoundingBox, Centroid, etc.) are mimicked in a custom function called *RegionOfInterest*, where each field of the structure becomes a property of the custom class. We added additional properties for storing state information and data associated with each ROI, along with a number of methods for comparing, merging, manipulating, and visualizing the single-frame and multi-frame ROIs. The single-frame to multi-frame ROI merging procedure is essentially a clustering process that merges single-frame ROIs together using such criteria as the proximity of their centroids, as well as proximity of their bounding-box (upper-left and lower-right corners). Performing this operation quickly was highly dependent on pre-grouping ROIs based on centroid location in overlapping blocks of the image frame, as well as grouping by size. This enabled the clustering to be performed in parallel (across CPU cores) followed by a second iteration of clustering to deal with redundancy in overlapping regions.

Once ROIs are established, all video data is reloaded and passed to a method in the *RegionOfInterest* class that extracts the 1-dimensional trace for each ROI representing the fluorescence intensity in that region over time. The ROIs and their traces can then be quickly visualized using another method in the *RegionOfInterest* class, which relies on the *distinguishable_colors* function, available on the Mathworks File Exchange (http://www.mathworks.com/matlabcentral/fileexchange/29702-generate-maximally-perceptually-distinct-colors/all_files).

Following ROI detection described above, we limited our dataset only to ROIs with minimal overlapping areas then refined the selected ROIs based on morphology and dynamic activity by the observers blinded to trial timing or events. Each trace was normalized with the following convention: $\Delta f = \frac{f - f_{avg}}{f_{avg}}$.

Removal of Overlapping and Over-dense ROIs

Our software was parameterized to maximize the number of possible ROIs generated from a imaging plane where numerous pixels were common to cells overlapping in depth. Averagely, around 1000–1300 ROIs were identified in each experiment session. In particular, cells that present greater spatial overlaps often have significant temporally coincident fluorescence signals. Hence, a local cluster-based workflow was designed to reduce the number of ROIs detected by imaging processing, using their morphology, cluster size and local overlap.

First, the ROIs of relatively large eccentricity, and of size on the extreme ends in the population were removed, because ROIs too deviant from circular shape or too small are morphologically less possibly a representation of a neuron. And the ROIs of too large size might be the combination of multiple cells sharing synchronized fluorescence signal dynamics. Then, the isolated ROIs were registered to be included in the final output.

In the second step, the remaining non-isolate ROIs were divided into local overlapping clusters of ROIs. Within each cluster, every ROI was scored using its size and two factors: overlap factor – the ratio between the overlapping area within it and its size, distance factor – the sum of the distance from its centroid to the centroids of other ROIs in the same cluster divided by the radius of the cluster. The score of the ROI was calculated as the overlap factor divided by the product of size and distance factor, i.e. score=percentage of overlap/[size× (sum of distance to the other ROIs/cluster radius)] ROIs with less score are considered better prediction of real neurons. The algorithm favors ROIs that have low percentage of overlap, and penalize those of too small size and close to the other ROIs in the same cluster.

Finally, the ROIs in the cluster were thresholded to be included in the final output. If there are more than 6 ROIs in a cluster, only the ROIs whose scores rank less than 60% of the ROIs', and whose overlap factors are less than 0.6 are kept. If there are 4 or 5 ROIs in the cluster, the ROIs whose scores' common logarithm is no more than 1 plus the common logarithm of least score within the cluster, and whose overlap factors are less than 0.5 are kept. When there are 2 or 3 ROIs in the cluster: if the number of ROIs with overlap factors less than 0.4 is more than 3, ROIs other than the two with the largest overlap factors were picked; if the number of ROIs with overlap factors less than 0.4 is 2, ROIs except the one with the largest overlap factors were picked.

On average, 64.38±7.91 (mean±SD) % of the ROIs remains after the removal (Fig. 2.2).

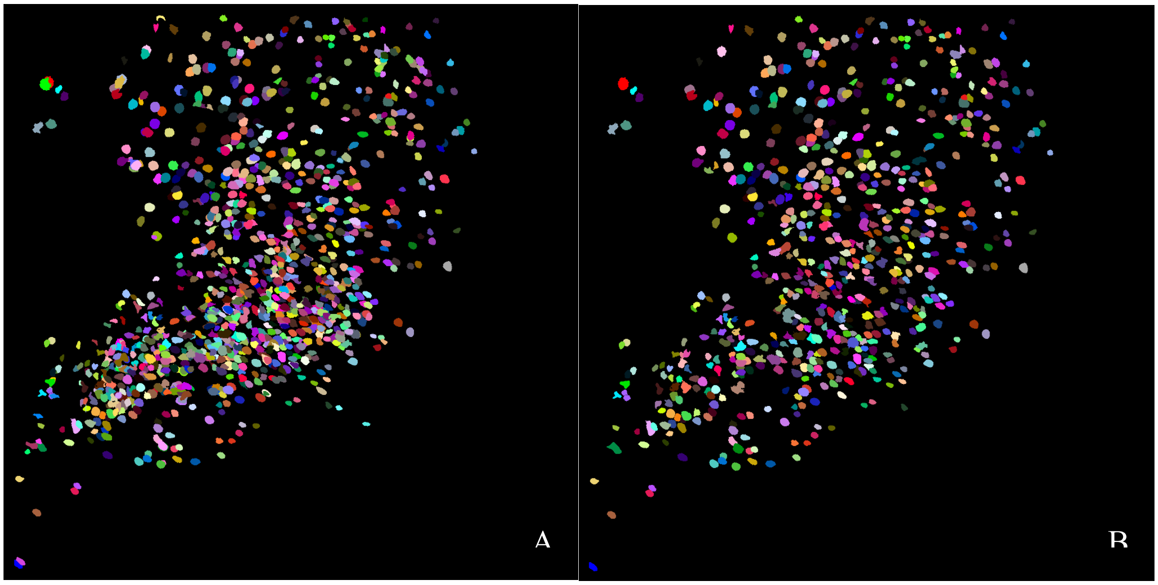

Figure 2.2. Pseudo-color localization of identified ROIs: (A) 1086 ROIs identified by the automatic software with heavy overlapping. (B) 665 ROIs generated by further rejection algorithm based morphology and geometric evaluation of overlapping clusters.

Deconvolution for Spike Inference from Calcium-imaging Signal

Typical in vitro data suggest that a reasonable first-order model may be constructed by convolving the spike train measurement with an exponential and adding Gaussian noise to simulate the calcium-imaging fluorescence signal (Vogelstein *et al.*, 2010).

Vogelstein *et al.* (2010) proposed an algorithm that can be used to the spike train inference underlying the observed calcium signal of the ROIs:

$$F_t = \alpha[Ca^{2+}]_t + \beta + \sigma\epsilon_t, \epsilon_t \sim \mathcal{N}(0,1)$$

$$[Ca^{2+}]_{t+1} = \left(1 - \frac{\Delta}{\tau}\right)[Ca^{2+}]_t + \frac{\Delta}{\tau}[Ca^{2+}]_b + An_t$$

where F_t represents the observed fluorescence signal trace and $[Ca^{2+}]_t$ represents the calcium concentration in the neuron. n_t indicates the possible number of spikes inferred on each frame of image. $[Ca^{2+}]_b$is the baseline calcium concentration. α and A are respectively the calcium and $\beta + \sigma\epsilon_t$ is a calcium-independent Gaussian noise in the fluorescence signal. Δ is the reciprocal of the sampling frequency of the fluorescence signal, and τ is the time constant which describes the exponential decay of calcium concentration in the cell.

Due to the linear relation among the variables, the model is over parameterized, and some parameters in the second equation can be absorbed into the first equation. By replacing $[Ca^{2+}]_t$ with its putative counterparts C_t after non-dimensionalization, we have:

$$F_t = \alpha C_t + \beta + \sigma\epsilon_t, \epsilon_t \sim \mathcal{N}(0,1)$$

$$C_t = \gamma C_{t-1} + n_t, \gamma = 1 - \frac{\Delta}{\tau}$$

Suppose the prior probability of a pike follows an exponential distribution $P(n_t) = \lambda\Delta e^{-n_t\lambda\Delta}$, which acts as an alternative for Poisson distribution. Given $\boldsymbol{F} = \{F_1, F_2, \dots, F_T\}$, our goal is to find the most likely spike train:

$$\hat{\boldsymbol{n}} = \underset{n_t}{\operatorname{argmax}} P(\boldsymbol{n}|\boldsymbol{F})$$

Because $P(\boldsymbol{n}|\boldsymbol{F}) = \frac{P(\boldsymbol{n},\boldsymbol{F})}{P(\boldsymbol{F})} = \frac{P(\boldsymbol{F}|\boldsymbol{n})P(\boldsymbol{n})}{P(\boldsymbol{F})}$ and $P(\boldsymbol{F})$ merely acts as a scaling factor,

$$\hat{\boldsymbol{n}} = \underset{n_t}{\operatorname{argmax}} P(\boldsymbol{F}|\boldsymbol{n})P(\boldsymbol{n})$$

Due to

$$P(\boldsymbol{F}|\boldsymbol{n}) = P(\boldsymbol{F}|\boldsymbol{C}) = \prod P(\boldsymbol{F}_t|\boldsymbol{C}_t) = \prod \mathcal{N}(\alpha C_t + \beta, \sigma^2)$$

$$P(\boldsymbol{n}) = \prod P(\boldsymbol{n}_t) = \prod \lambda \Delta e^{-n_t \lambda \Delta}$$

we have

$$\hat{\boldsymbol{n}} = \underset{n_t}{\operatorname{argmax}} \prod \left[\frac{1}{\sqrt{2\pi\sigma^2}} e^{-\frac{1}{2}\frac{(F_t - \alpha C_t - \beta)^2}{\sigma^2}} \lambda \Delta e^{-n_t \lambda \Delta} \right]$$

Taking the logarithm renders

$$\hat{\boldsymbol{n}} = \underset{n_t}{\operatorname{argmax}} \sum -\frac{1}{2\sigma^2}(F_t - \alpha C_t - \beta)^2 - n_t \lambda \Delta$$

While $n_t = C_t - \gamma C_{t-1}$, we can estimate $\boldsymbol{C}$ instead

$$\hat{\boldsymbol{C}} = \underset{C_t}{\operatorname{argmax}} \sum -\frac{1}{2\sigma^2}(F_t - \alpha C_t - \beta)^2 - (C_t - \gamma C_{t-1}) \lambda \Delta$$

In order to solve the problem, interior-point method should be adopted because the sharp threshold imposed by the non-negativity constraint prohibits the use of standard gradient ascent techniques. Interior-point methods solve nondifferentiable problems indirectly by solving a series of differentiable subproblems that converge to the solution of the original nondifferentiable problem. In particular, each subproblem within the series adds a weighted barrier term that approaches to negative infinity as n_t approaches zero. Iteratively reducing the weight of the barrier term guarantees convergence to the correct threshold. Thus,

$$\hat{\boldsymbol{C}}_z = \underset{\boldsymbol{C}}{\operatorname{argmax}} \sum -\frac{1}{2\sigma^2}(F_t - \alpha C_t - \beta)^2 - (C_t - \gamma C_{t-1}) \lambda \Delta + z \ln(C_t - \gamma C_{t-1})$$

Rewrite the equation in matrix form:

$$MC = \begin{bmatrix} -\gamma & 1 & 0 & 0 & \cdots & 0 \\ 0 & -\gamma & 1 & 0 & \cdots & 0 \\ \vdots & \ddots & \ddots & \ddots & \ddots & \vdots \\ 0 & \cdots & 0 & -\gamma & 1 & 0 \\ 0 & \cdots & 0 & 0 & -\gamma & 1 \end{bmatrix} \begin{bmatrix} C_1 \\ C_2 \\ \vdots \\ C_{T-1} \\ C_T \end{bmatrix} = \begin{bmatrix} n_1 \\ n_2 \\ \vdots \\ n_{T-1} \end{bmatrix}$$

let $\mathbf{1}$ be a $(T-1)$-dimension column vector, $\boldsymbol{\beta}$ be a T-dimension column vector of β values, and $\boldsymbol{\lambda} = \lambda\Delta\mathbf{1}$. Using superscript I to indicate element wide operation,

$$\widehat{\boldsymbol{C}}_z = \underset{\boldsymbol{MC} \geq^I \mathbf{0}}{\operatorname{argmax}} \sum -\frac{1}{2\sigma^2} \|\boldsymbol{F} - \alpha\boldsymbol{C} - \boldsymbol{\beta}\|_2^2 - (\boldsymbol{MC})^T\boldsymbol{\lambda} + z \ln_I(\boldsymbol{MC})^T\mathbf{1}$$

Then we use Newton-Raphson method to ascend a surface. After iteratively computing the gradient $\boldsymbol{g}$ the Hessian $\boldsymbol{H}$ of the argument to be maximized with respect to $\boldsymbol{C}$,

$$\boldsymbol{g} = -\frac{1}{\sigma^2}(\boldsymbol{F} - \alpha\boldsymbol{C} - \boldsymbol{\beta}) + \boldsymbol{M}^T\boldsymbol{\lambda} - z\boldsymbol{M}^T(\boldsymbol{MC})^{-1^I}$$

$$\boldsymbol{H} = \frac{\alpha^2}{\sigma^2}\boldsymbol{I} + z\boldsymbol{M}^T(\boldsymbol{MC})^{-1^I}\boldsymbol{M}$$

We update $\boldsymbol{C}_z \leftarrow \boldsymbol{C}_z + s\boldsymbol{d}$, while s refers to the step size and $\boldsymbol{d}$ is the step direction obtained by solving $\boldsymbol{Hd} = \boldsymbol{g}$.

In the model, the parameters $\boldsymbol{\theta} = \{\alpha, \beta, \sigma, \gamma, \lambda\}$ might be unknown. The algorithm to estimate the most likely parameters $\widehat{\boldsymbol{\theta}}$ includes initializing some estimate of the parameters, and then recursively computing $\widehat{\boldsymbol{n}}$ until some convergence criterion is reached.

To initialize the parameters, we first map the observed fluorescence trace according to its scale: $\boldsymbol{F} \leftarrow \frac{\boldsymbol{F} - F_{min}}{F_{max} - F_{min}}$. Hence, α can be set to 1, and β can be set to the median of $\boldsymbol{F}$. σ can be initialized as the median absolute deviation, commonly used as an estimator of the SD of a normal distribution, of $\boldsymbol{F}$: $\sigma = \frac{\mathrm{median}_t(F_t - \mathrm{median}_s(F_s))}{K}, K = 1.4785$. γ is initialized at $1 - \frac{\Delta}{1\ \mathrm{sec}}$, and λ at 1 Hz.

Ideally, we can integrate out the hidden variable to find the most likely parameters:

$$\widehat{\boldsymbol{\theta}} = \operatorname*{argmax}_{\boldsymbol{\theta}} \int P(\boldsymbol{F}, \boldsymbol{C}|\boldsymbol{\theta}) d\boldsymbol{C} = \operatorname*{argmax}_{\boldsymbol{\theta}} \int P(\boldsymbol{F}|\boldsymbol{C}; \boldsymbol{\theta}) P(\boldsymbol{C}|\boldsymbol{\theta}) d\boldsymbol{C}$$

Because the integration is easily tractable, we can simply approximate the parameters by the MLE given the MAP estimate of the hidden variable:

$$\widehat{\boldsymbol{\theta}} = \operatorname*{argmax}_{\boldsymbol{\theta}} P\left(\boldsymbol{F}, \widehat{\boldsymbol{C}}\middle|\boldsymbol{\theta}\right) = \operatorname*{argmax}_{\boldsymbol{\theta}} P\left(\boldsymbol{F}\middle|\widehat{\boldsymbol{C}}; \boldsymbol{\theta}\right) P\left(\boldsymbol{n}\middle|\widehat{\boldsymbol{\theta}}\right)$$

$$= \operatorname*{argmax}_{\boldsymbol{\theta}} \ln P\left(\boldsymbol{F}\middle|\widehat{\boldsymbol{C}}; \boldsymbol{\theta}\right) + \ln P\left(\boldsymbol{n}\middle|\widehat{\boldsymbol{\theta}}\right)$$

$$\ln P\left(\boldsymbol{F}\middle|\widehat{\boldsymbol{C}}; \boldsymbol{\theta}\right) + \ln P\left(\boldsymbol{n}\middle|\widehat{\boldsymbol{\theta}}\right) = \sum \ln P\left(F_t\middle|\hat{C}_t; \alpha, \beta, \sigma\right) + \sum \ln P(n_t|\lambda)$$

Hence,

$$\left\{\hat{\alpha}, \hat{\beta}, \hat{\sigma}\right\} = \operatorname*{argmax}_{\alpha,\beta,\sigma} \sum \ln P\left(F_t\middle|\hat{C}_t; \alpha, \beta, \sigma\right) = \operatorname*{argmax}_{\alpha,\beta,\sigma} \sum \ln \mathcal{N}(\alpha C_t + \beta, \sigma^2)$$

$$= \operatorname*{argmax}_{\alpha,\beta,\sigma} \sum -\frac{1}{2} \ln 2\pi\sigma^2 - \frac{1}{2}\left(\frac{F_t - \alpha\hat{C}_t - \beta}{\sigma}\right)^2$$

Taking the gradient with respect to α and β and setting them to zero respectively leads to:

$$\begin{cases} \hat{\alpha} \sum \hat{C}_t + T\hat{\beta} = \sum F_t \\ \hat{\alpha} \sum \hat{C}_t^2 + \hat{\beta} \sum \hat{C}_t = \sum F_t \hat{C}_t \end{cases} \xrightarrow{yields} \begin{cases} \hat{\alpha} = \dfrac{\sum \hat{C}_t \sum F_t - T \sum F_t \hat{C}_t}{\left(\sum \hat{C}_t\right)^2 - T \sum \hat{C}_t^2} \\ \hat{\beta} = \dfrac{\sum \hat{C}_t^2 \sum F_t - \sum \hat{C}_t \sum F_t \hat{C}_t}{T \sum \hat{C}_t^2 - \left(\sum \hat{C}_t\right)^2} \end{cases}$$

Taking the gradient with respect to σ and setting it to zero leads to:

$$\hat{\sigma} = \sqrt{\frac{1}{T}\sum\left(F_t - \hat{\alpha}\hat{C}_t - \hat{\beta}\right)^2}$$

Finally,

$$\hat{\lambda} = \underset{\lambda}{\operatorname{argmax}} \sum \ln P(n_t|\lambda) = \underset{\lambda}{\operatorname{argmax}} \sum \ln(\lambda \Delta) - \hat{n}_t \lambda \Delta$$

Taking the gradient with respect to λ and setting it to zero leads to:

$$\hat{\lambda} = \frac{T}{\Delta \sum \hat{n}_t}$$

Gaussian-Process Factor Analysis (GPFA)

Gaussian-Process Factor Analysis (Yu *et al.*, 2009) simultaneously performs the smoothing and dimensionality-reduction operations in a unified common probabilistic framework. Rather different from traditional statistic dimensionality-reduction techniques, for instance, Principle Component Analysis (PCA) and Factor Analysis, which takes into no account time labels when applied to time series data, GPFA leverages the time label information to provide more powerful dimensionality reduction for time series data. The GPFA model is simply a set of factor analyzers (one per time point, each with identical parameters) that are linked together in the low-dimensional state space by a Gaussian process (GP) prior. A Gaussian process is a statistical distribution $X_t, t \in T$, for which any finite linear combination of samples has a joint Gaussian distribution. Introducing the GP allows for the specification of a correlation structure across the low-dimensional states at different time points. For example, if the system evolves smoothly over time, we can specify that the system's state should be more similar between nearby time points than between those faraway.

Prior to GPFA, the spike trace is square-root transformed in order to stabilize the noise variance (Yu *et al.*, 2009), because GPFA assumes stationary noise variance, which might not be the case for spike trace data; for neurons, their firing rate can change drastically in response to stimulus. Square-root transform has been known to stabilize Poison-distributed counts (Kihlberg *et al.*, 1972), which, though, in the calcium fluorescence deconvolution model, is simulated by using exponential distribution for computational convenience.

Let the original neural data set be the high-dimensional vector of square-tooted spike inference traces, $\mathbf{y}_{:,t} \in \mathbb{R}^{q\times 1}$, at time point of $t = 1, \dots, T$, where q is the number of neurons. We seek to extract a corresponding low-dimensional latent neural state, $\mathbf{x}_{:,t} \in \mathbb{R}^{p\times \mathbf{1}}$, where p is the dimensionality of the state space ($p < q$). We then define the neural states of all time points into a neural trajectory in a matrix fashion $X = \left[\mathbf{x}_{:,1}, \dots \mathbf{x}_{:,T}\right] \in \mathbb{R}^{p\times T}$. Similarly, the original observations can be presented as $Y = \left[\mathbf{y}_{:,1}, \dots \mathbf{y}_{:,T}\right] \in \mathbb{R}^{p\times T}$. We define a linear Gaussian relationship between the observations $\mathbf{y}_{:,t}$ and the neural states $\mathbf{x}_{:,t}$:

$$\mathbf{y}_{:,t}|\mathbf{x}_{:,t} \sim \mathcal{N}\left(C\mathbf{x}_{:,t} + \mathbf{d}, R\right)$$

where $C \in \mathbb{R}^{q\times p}$, $\mathbf{d} \in \mathbb{R}^{q\times 1}$ and $R \in \mathbb{R}^{q\times q}$ are model parameters to be learned. We constrain the covariance matrix R to be diagonal, where the diagonal elements are independent noise variances of each neuron.

To smoothen the neural trajectories, we relate the neural states $\mathbf{x}_{:,t}$ at different time points through GPs. We define a separate GP for each dimension of the state space with indices $i = 1, \dots, p$

$$\mathbf{x}_{i,:} \sim \mathcal{N}(\mathbf{0}, K_i)$$

where $\mathbf{x}_{i,:} \in \mathbb{R}^{1\times T}$ is the ith row of X and $K_i \in \mathbb{R}^{T\times T}$ is the covariance matrix for the ith GP. We choose the commonly used square exponential (SE) covariance function:

$$K_i(t_1, t_2) = \sigma_{f,i}^2 \exp\left(-\frac{(t_1 - t_2)^2}{2\tau_i^2}\right) + \sigma_{n,i}^2 \cdot \delta_{t_1,t_2}$$

where $K_i(t_1, t_2)$ denotes the (t_1, t_2)th entry of K_i, $t_1, t_2 = 1, \dots, T$. The SE covariance is defined by its signal variance $\sigma_{f,i}^2 \in \mathbb{R}_+$, characteristic time scale $\tau_i \in \mathbb{R}_+$ and GP noise variance, and GP variance $\sigma_{n,i}^2$. The Kroneker delta δ_{t_1,t_2} equals 1 if $t_1 = t_2$, and 0 otherwise.

Because the neural trajectories X are latent and inferred from the observations Y, the scale of X (defined by the K_i) is arbitrary. Hence, any scaling of X can be compensated by appropriately scaling C such that the scale of Y remains faithful to the sample. To remove this model redundancy without changing the expressive power of the model, we fix the scale of X and allow C to be learned without constraints. we set the prior distribution of the neural state $\mathbf{x}_{:,t}$ at each time point t to be $\mathcal{N}(\mathbf{0}, I)$ by fixing $K_i(t, t) = 1$ (however, note that the $\mathbf{x}_{:,t}$ are still correlated across different *t*). This can be achieved by setting $\sigma_{f,i}^2 = 1 - \sigma_{n,i}^2$, where $0 < \sigma_{n,i}^2 \leq 1$. Because we seek to extract smooth neural trajectories, we fixed $\sigma_{n,i}^2$ to a small value (10^{-3}), as is often done for GPs, which leaves τ_i the only parameter that needs to be learned.

To fit the GPFA model, we have to learn a set of parameters $\theta = \{C, \boldsymbol{d}, R, \tau_1, \dots, \tau_p\}$, which can be estimated by maximize the probability of the observed data Y in an expectation-maximization algorithm.

Once the GPFA model is learned, we can use it to extract neural trajectories $E[X|Y]$ from the observed activity Y. If we concatenate the columns of X as $\bar{\mathbf{x}} = \left[\mathbf{x}'_{:,1}, \ldots, \mathbf{x}'_{:,T}\right]' \in \mathbb{R}^{pT\times 1}$, and Y as $\bar{\mathbf{y}} = \left[\mathbf{y}'_{:,1}, \ldots, \mathbf{y}'_{:,T}\right]' \in \mathbb{R}^{qT\times 1}$, we can express the GPFA model as

$$\bar{\mathbf{x}} \sim \mathcal{N}(\mathbf{0}, \bar{K})$$

$$\bar{\mathbf{y}}|\bar{\mathbf{x}} \sim \mathcal{N}\left(\bar{C}\bar{\mathbf{x}} + \bar{\mathbf{d}}, \bar{R}\right)$$

where the block diagonal matrices $\bar{C} \in \mathbb{R}^{qT\times pT}$ and $\bar{R} \in \mathbb{R}^{qT\times pT}$ comprise T blocks of C and R respectively. The vector $\bar{\mathbf{d}} \in \mathbb{R}^{qT\times 1}$ is a concatenation of T copies of $\mathbf{d}$. The covariance matrix $\bar{K} = \begin{bmatrix} \bar{K}_{11} & \cdots & \bar{K}_{1T} \\ \vdots & \ddots & \vdots \\ \bar{K}_{T1} & \cdots & \bar{K}_{TT} \end{bmatrix} \in \mathbb{R}^{pT\times pT}$ comprises blocks $\bar{K}_{t_1 t_2} = \mathbf{diag}\left\{K_1(t_1, t_2), \ldots, K_p(t_1, t_2)\right\} \in \mathbb{R}^{p\times p}$ and $t_1, t_2 = 1, \ldots, T$. In this notation, the joint distribution of $\bar{\mathbf{x}}$ and $\bar{\mathbf{y}}$ can be written as

$$\begin{bmatrix} \bar{\mathbf{x}} \\ \bar{\mathbf{y}} \end{bmatrix} \sim \mathcal{N}\left(\begin{bmatrix} \mathbf{0} \\ \bar{\mathbf{d}} \end{bmatrix}, \begin{bmatrix} \bar{K} & \bar{K}\bar{C}' \\ \bar{C}\bar{K} & \bar{C}\bar{K}\bar{C}' + \bar{R} \end{bmatrix}\right)$$

Using the basic result of conditioning for jointly Gaussian random variables

$$\bar{\mathbf{x}}|\bar{\mathbf{y}} \sim \mathcal{N}\left(\bar{K}\bar{C}'(\bar{C}\bar{K}\bar{C}' + \bar{R})^{-1}\left(\bar{\mathbf{y}} - \bar{\mathbf{d}}\right), \bar{K} - \bar{K}\bar{C}'(\bar{C}\bar{K}\bar{C}' + \bar{R})^{-1}\bar{C}\bar{K}\right)$$

Thus, the extracted neural trajectory is

$$E[\bar{\mathbf{x}}|\bar{\mathbf{y}}] = \bar{K}\bar{C}'(\bar{C}\bar{K}\bar{C}' + \bar{R})^{-1}\left(\bar{\mathbf{y}} - \bar{\mathbf{d}}\right)$$

and the data likelihood $P(Y)$ can be easily computed since $\bar{\mathbf{y}} \sim \mathcal{N}\left(\bar{\mathbf{d}}, \bar{C}\bar{K}\bar{C}' + \bar{R}\right)$.

The low-dimensional neural trajectories can be related to the high-dimensional observed activity by $\mathbf{y}_{:,t}|\mathbf{x}_{:,t} \sim \mathcal{N}\left(C\mathbf{x}_{:,t} + \mathbf{d}, R\right)$, which defines a linear mapping C between the two spaces. Each column of C defines an axis in the high-dimensional space. The ith element of $\boldsymbol{x}_{:,t}$ $(i = 1, \dots, p)$ specifies "how far to go" along the axis defined by the ith column of C. The location in the high-dimensional space corresponding to the neural state $\mathbf{x}_{:,t}$ is given by the summed contributions along each of the p aforementioned axes, plus a constant offset $\boldsymbol{d}$.

To make the visualization of the neural trajectories more intuitive, we need to orthonormalize the columns of C. By finding a set of orthonormal basis vectors spanning the same space as the columns of C, the orthonormalization procedure does not alter the GPFA model-fitting procedure nor the extracted neural trajectories; it simply offers a more intuitive way of visualizing the extracted trajectories.

We can apply the singular value decomposition to the learned C, rendering $C = UDV'$, where $U \in \mathbb{R}^{q\times p}$ and $V \in \mathbb{R}^{p\times p}$ each have orthonormal columns and $D \in \mathbb{R}^{p\times p}$ is diagonal. Thus, we can write $C\mathbf{x}_{:,t} = U\left(DV'\mathbf{x}_{:,t}\right) = U\tilde{\mathbf{x}}_{:,t}$, where $\tilde{\mathbf{x}}_{:,t} = DV'\mathbf{x}_{:,t} \in \mathbb{R}^{p\times 1}$ is the orthonormalized neural state at time point t. The orthonormalized neural trajectory extracted from the observed activity Y is thus $DV'E[X|Y]$. Since U has orthonormal columns, we can intuitively visualize the trajectories extracted by GPFA similarly as those done by PCA. Even the elements of $\tilde{\mathbf{x}}_{:,t}$ and the corresponding columns of U can be ordered by the amount of data covariance explained, analogous to PCA, which is made possible by the singular value decomposition.

DECONVOLUTION OF CALCIUM FLUORESCENCE SIGNAL

Due to the slow exponential time-course of GCaMP6f's post-response signal (Badura *et al*., 2014; Chen *et al*., 2013), which might contribute to unexpected correlation between neuronal signals, GPFA cannot be directly applied to the GCaMP data set. Thus, the fast nonnegative deconvolution method (Vogelstein *et al.*, 2010) is used to estimate the spike train inference prior to application of dimension reduction.

Removal of Inactive Neurons

Naturally, we are only interested the neurons that indeed fire. Thus, it is essential to remove those who show trivial spike activity throughout the experiment. Besides, in the GPFA model, the fitted observation noise for a low-firing rate unit will be small, so the neural trajectory may show a deflection each time the neuron spikes (Yu *et al.*, 2009).

First, we set a reasonable threshold (0.5), below which, at each frame we identify the neuron as inactive if its spike inference is. Because we assumed the spike inference follows an exponential distribution, we then calculated the rate parameter of such an exponential distribution whose 99 percentile is the threshold. Using random simulation, we were able to generate a distribution for the number of frames where the spike inference is less than the threshold given the total period of the data time series. Finally, we took the 95 percentile of this distribution. If one neuron's number of inactive frames is more than the 95 percentile, it will be disqualified for the following analysis (Fig. 3.2) and GPFA.

Baseline Normalization

We performed baseline normalization to extract time-varying fluorescence changes. The normalization of fluorescence and spike time courses for each neuron in Fig. 3.2 consists two steps, z-core and t-score. First, within each trial, the mean and standard deviation are calculated for each neuron over the baseline period, using which, the whole trace is z-scored. Then, for each neuron, the mean for each trace was computed over the baseline period, generating a set of elements as many as the number of trials representing the average baseline level. By comparing the multi-trial set of each time point (including the baseline) to the baseline average set, we were able to collapse the traces of all the trials into a single time series of t-scores.

Spike Inference Captured Neuronal Dynamics During Behavior

The deconvolution algorithm was able to reveal the dynamics of spike activity underlying the calcium fluorescence response. One can interpret the time course of spike inference as the evolution of relative probability (arbitrary unit) of the neuron spiking at one time point given the whole fluorescence trace.

Fig. 3.1 shows a neuron increases its firing rate in response to the stimulus in correct trials, but its activation is less associated with the delivery of air puff. Despite the average long exponential off-response decrease of the fluorescence signal, which lasts longer than 2 s after the stimulus, the average spike inference is restrained within the stimulation-air puff interval (Fig. 3.1). On the other hand, similar reaction dynamics is absent in incorrect trials.

The slow off-response exponential dynamics of the calcium fluorescence manifests as sustained smear through time for neurons with multiple firings after the stimulation (Fig. 3.2A), making it hard to differentiate consecutive spikes separated only by a very short amount of time. Once the fluorescence trace is deconvolved, it is easy to spot two incidences of population spikes related to the task, one aligned to the sound, and the other to the air puff (Fig. 3.2B).

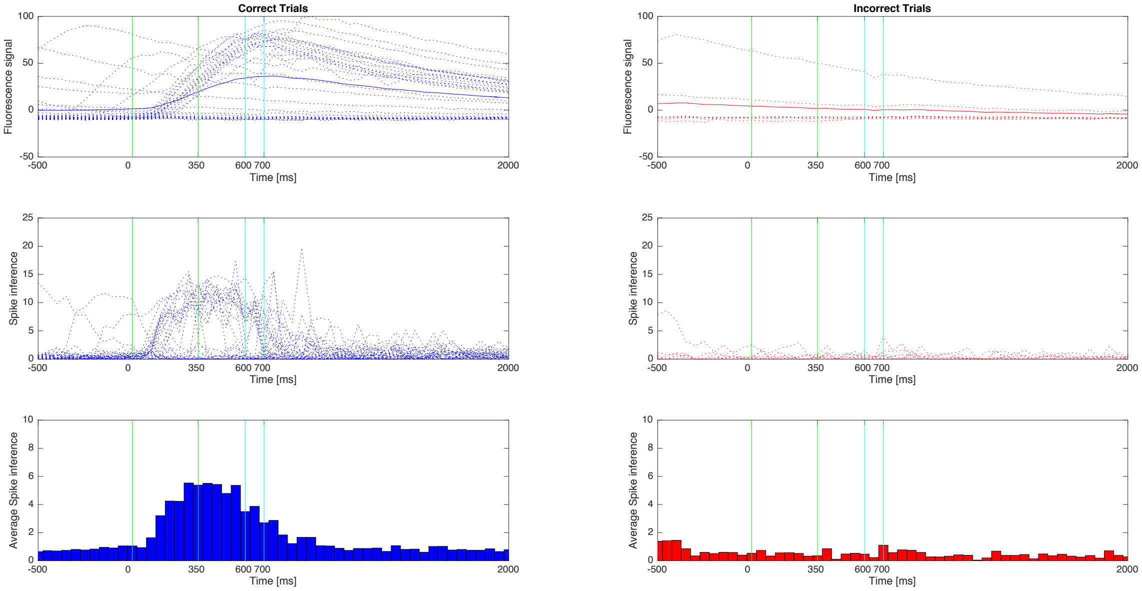

Figure 3.1. Calcium signal and corresponding spike inference of the same neuron in correct and incorrect trials: The dotted lines in the fluorescence signal figures and the spike inference figures represent the individual traces for each trial. The solid lines in the fluorescence signal figures represent the average trace over all trials of the same type. The bar graphs represent the average spike train inference over all trials of the same type. Time zero marks the onset of sound stimulation.

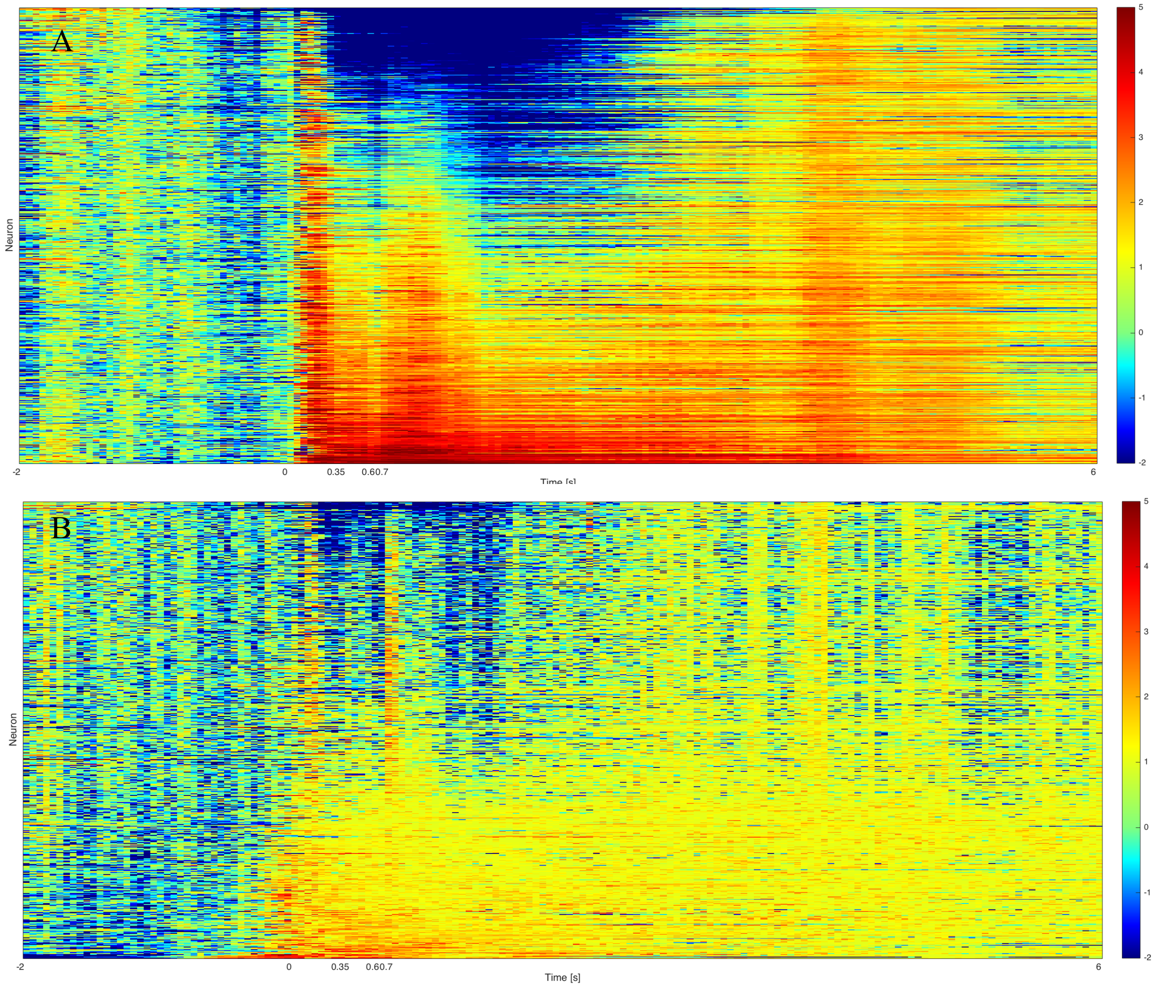

Figure 3.2. Normalized calcium signal and corresponding spike train inference of multiple neurons for all the trials in one experiment session: (A) 537 neuros sorted by their average fluorescence signal intensity within the first 2 s after the tone, highest to lowest from bottom to top. (B) 537 neurons sorted by their average spike inference probability within the first 2 s after the tone, highest to lowest from bottom to top. Time zero marks the onset of sound stimulation. The color represents baseline-normalized activity intensity of the neuron.

Discussion

Vogelstein's (2010) model was originally developed to deconvolve OGB-1fluorecence signal, whose decay shows a single exponential fit. However, GCaMP6f can respond with a double exponential time course, though the improvement by using double exponential fits was very limited (Storace *et al.*, 2015). These factors may have slightly impact on the reliability of the deconvolution algorithm when being applied to our GCaMP6f data set.

DIMENSION REDUCTION ANALYSIS USING GPFA

Using GPFA for exploratory data analysis and visualization, we were able to observe the change of network dynamics of the hippocampus neurons through days of learning in the low-dimension representations. The neural trajectories in the low-dimension projection also suggested interesting features of the population high-dimension time series, and hence, offered constructive strategy in statistical analysis of the high-dimension data.

Analogue Measurement of Eye Squint

Binary differentiation of correct and incorrect trials is every intuitive, but very sensitive to thresholding methods and corresponding parameters. Thus, quantification of the eye squint movement is another way to describe the behavior of the trial, and can be essential, if not only compensatory.

For each trial, we first calculate the sum of absolute value of first derivative of reflection values during the 600 ms response trace interval. After defining the baseline as from 15 s after the previous trial until the initiation of the current trial, we generate a distribution of the sum of absolute value of first derivative during a random 600 ms period within the baseline, and acquire the mean and standard deviation. Then we can z-score the response-interval sum of absolute value of first derivative. In this way, one iteration of z-scoring is finished. Averaging multiple iterations then results in the analogue indication of eye squint for the trial.

Removal of Cross-talking Signals

Crosstalk between ROIs, which can be caused by ROIs being overlapping, may lead different neurons have identical (or nearly the same) activity on each trial. Because the neural trajectory attempts to capture correlated activity across the neural population, it will identify the shorted ROIs as being strongly correlated and dedicate a latent dimension to those neurons (Yu *et al.*, 2009). We can solve this problem by looking at the eigenvalues and eigenvectors of the covariance matrix of the population traces. After finding the eigenvalues with extremely small values, we can identify the extremely large elements in the corresponding eigendirection, and corresponding neurons could be corruptive due to cross-talking.

Low Dimension Representations Paralleled Learning Performance

For each session of learning, which usually happens on different days, the data were projected to a 10-dimension space using GPFA. Compared to the high-dimension data space, 10 dimensions can explain 49.59 ± 27.92 % of the variance. As learning proceeded, the correct rates from the first day of learning to the last day of learning are 0.500, 0.613, 0.688 and 0.825 for the animal shown below.

On the first day of learning, the neural trajectories do not show too many informative features along their time course, nor can the trials be differentiated as correct or incorrect by evaluating the trajectories (Fig. 4.1A&B). Although, we can still see after the stimulation onset, the network does start to respond, and can even take very sharp reaction upon air puff delivery (Fig. 4.1A&B).

On the last day of learning, the low-dimension projections of the data present more unique characteristics in different dimensions. For instance, in dimension 4, the neural state of the network shows rapid response after the onset of the sound. In addition, this dimension is also tightly related to the delivery of air puff. Thus, this dimension is characterized by very dynamic response dependent on the external stimulations (Fig. 4.1C, Fig. 4.2C). On the other hand, dimension 5 is more associate with the outcome of the trial, i.e. correct and incorrect trials (Fig. 4.1D). Most of the time series of the incorrect trials in this dimension tend to dive below zero after the tone onset, while the average response trajectories of the correct trials evolve above zero. In addition, below-zero evolution also predominates trajectories accompanied by low squint intensity (Fig. 4.2D). However, a considerable number of correct trajectories also lie below zero (Fig. 4.1D), which might imply that other internal process may involve the hippocampal neural network in spite of the unanimous nominal final output.

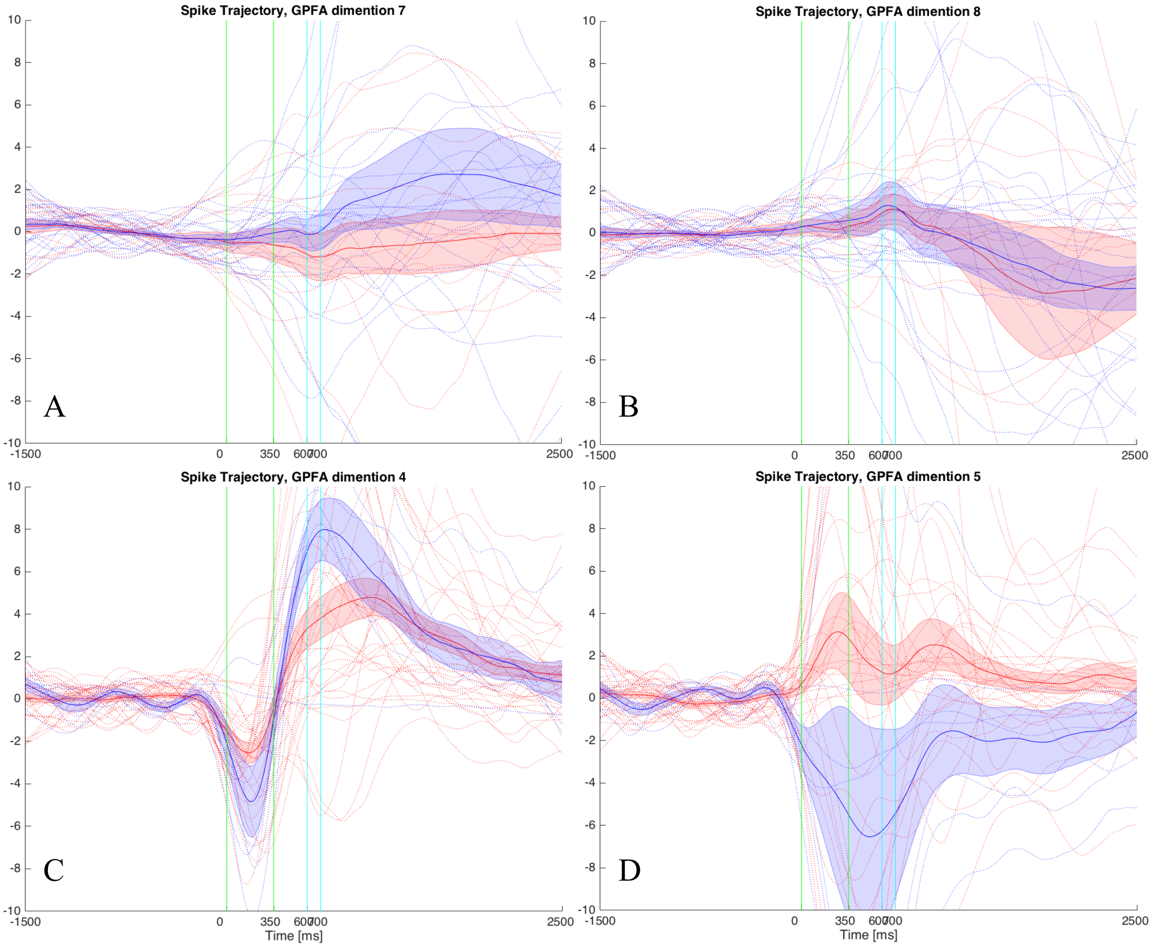

Figure 4.1. Temporal evolution of neural state in single dimensions: (A) Neural trajectories of trials on the first day of learning in the 7th dimension extracted by GPFA. (B) Neural trajectories of trials on the first day of learning in the 8th dimension extracted by GPFA. (C) Neural trajectories of trials on the last day of learning in the 4th dimension extracted by GPFA. (D) Neural trajectories of trials on the last day of learning in the 5th dimension extracted by GPFA. The dimensions presented were chosen arbitrarily, yet without losing their representativeness. Red color represents correct trials, and blue is for incorrect trials. Each dotted curve represents an individual trial. The solid line and the corresponding shaded area marks the average trajectory and the error (mean±SEM). Time zero refers to the onset of the sound.

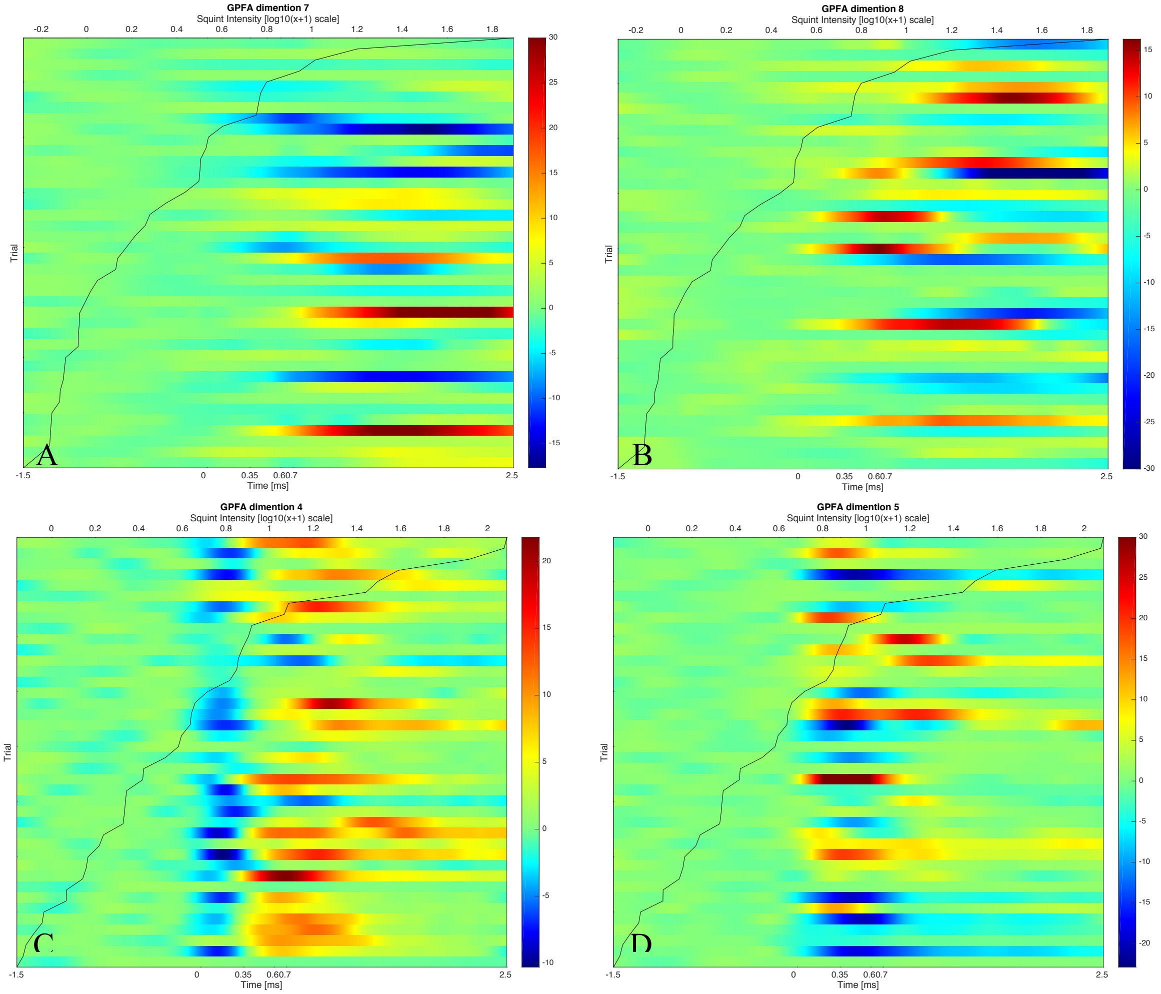

Figure 4.2. Temporal evolution of neural state of individual trials in single dimensions superimposed with squint intensity: (A) Neural trajectories of trials on the first day of learning in the 7th dimension extracted by GPFA, superimposed by the corresponding squint intensity. (B) Neural trajectories of trials on the first day of learning in the 8th dimension extracted by GPFA, superimposed by the corresponding squint intensity. (C) Neural trajectories of trials on the last day of learning in the 4th dimension extracted by GPFA, superimposed by the corresponding squint intensity. (D) Neural trajectories of trials on the last day of learning in the 5th dimension extracted by GPFA, superimposed by the corresponding squint intensity. The dimensions presented were chosen arbitrarily, yet without losing their representativeness. Time zero refers to the onset of the sound. A transform $\mathbf{log_{10}(x+1)}$ is applied to the squint intensity. The trials are sorted by squint intensity.

Typical neural trajectories in a 2D plane comprise the initiation of movement after the tone onset, and returning to the start point (Fig. 4.3). The start point is defined as the average center of all the baseline neural states across all trials. The trajectories tend to begin swirling back to the start point more early once the behavior has been learned (Fig. 4.3). On the last day of learning, the trajectories have already begun approaching the turning point upon the end of the sound stimulation, and by 0.7 s have about to return to the start point (Fig. 4.3B). However, at 1.2 s, the neural trajectories on the first day of learning have yet to rewind (Fig. 4.3A).

The neural trajectories also travel faster and further once the animal has associated the sound with the air puff (Fig. 4.4), which is also true in the high-dimension space (defined by the number of neurons) (Fig. 4.5A). The neural trajectories also reach its furthest point more early on the last day of learning than the first day (Fig. 4.4A&C) as the trajectories also experience a much more delayed acceleration on the first day of learning (Fig. 4.4B&D).

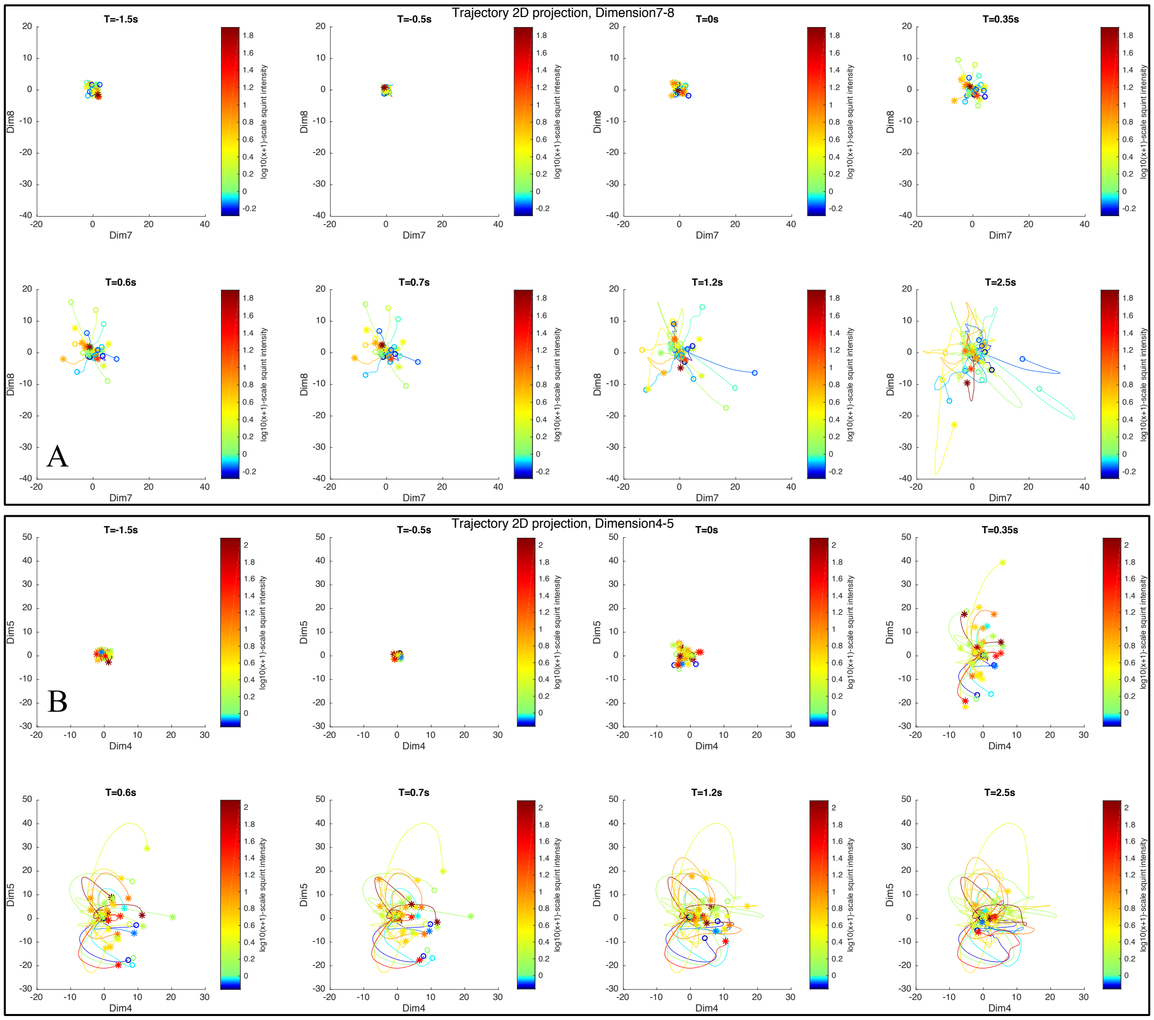

Figure 4.3. Snapshots of 2D neural trajectories evolution at different time point: (A) 2D neural trajectories' evolution on the first day of learning. (B) 2D neural trajectories' evolution on the first day of learning. The dimensions presented were chosen arbitrarily, yet without losing their representativeness. Each solid curve is the trajectory for an individual trial. The marker at the end of the curve indicates the current neural state at the time point when the snapshot is taken. * indicates correct trials; ○ indicates incorrect trials. The color represents squint intensity, which a transform $\mathbf{\log_{10}(x+1)}$ is applied to.

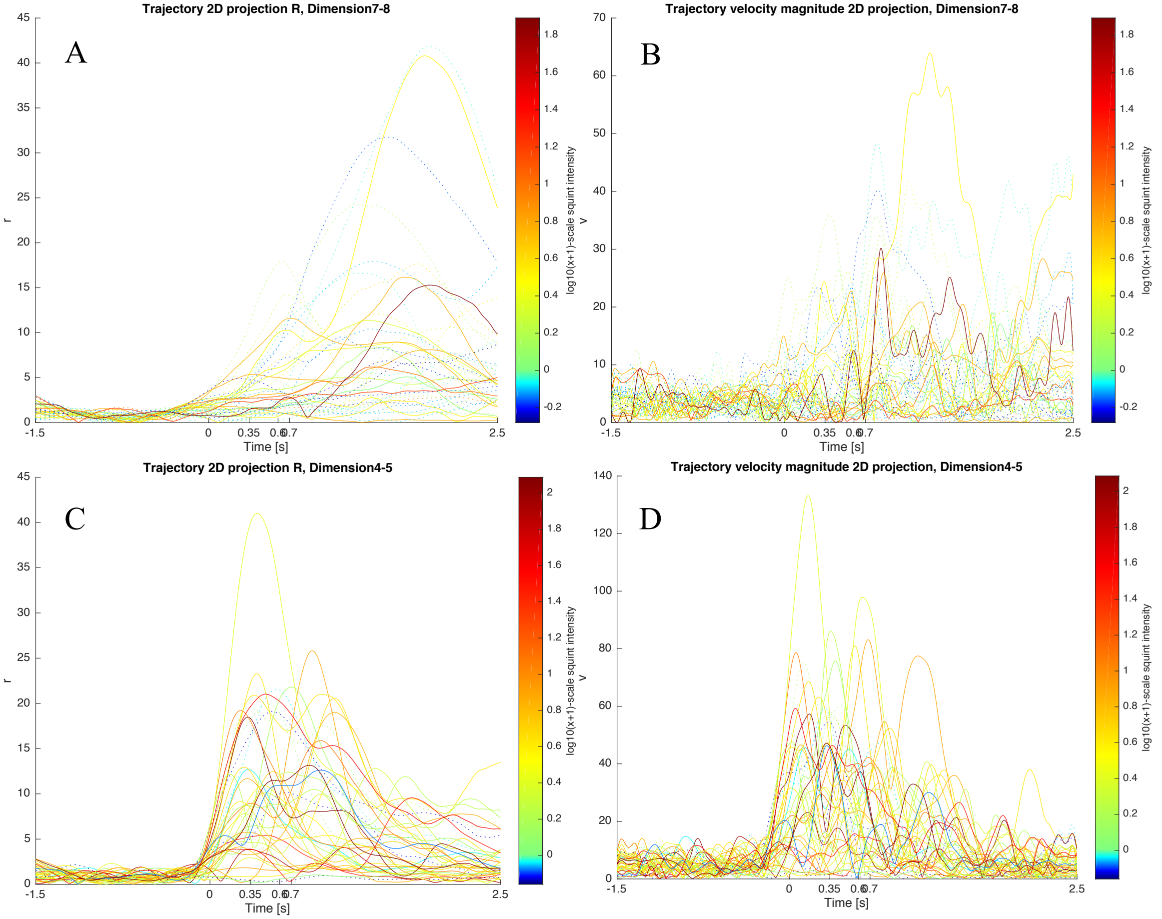

Figure 4.4. Temporal evolution of 2D neural trajectory's distance from starting point and its speed: (A) 2D neural trajectories' evolution of distance from the starting point on the first day of learning. (B) 2D neural trajectories' speed evolution of distance from the starting point on the first day of learning. (C) 2D neural trajectories' evolution of distance from the starting point on the last day of learning. (D) 2D neural trajectories' speed evolution of distance from the starting point on the last day of learning. The dimensions presented were chosen arbitrarily, yet without losing their representativeness. The solid curves represent the correct trials; the dotted curves represent the incorrect trials. The color indicates squint intensity, which a transform $\mathbf{log_{10}(x+1)}$ is applied to.

High-dimension Trajectory Features Vary with Learning Process

In the high-dimension space, when considering all the trials together, regardless of correct or incorrect, the neural trajectories return to a baseline initial sphere much faster, as having a shorter re-entrance time, if the animal has learned the behavior (Fig. 4.5A). For each trial, we bootstrapped the distance of the high-dimension neural state to the origin over the baseline period, and achieved a 90 percentile as the baseline sphere boundary. On the days when learning has happened, the trajectories start up much faster, with significantly greater sound onset-air puff interval speed compared to the first day of learning (Fig. 4.5A).

Overall, the dynamics of the hippocampal network shows drastic change when the animal learned the association between the stimulation and the air puff. The network deviates faster and further from the baseline status, in the meantime returning to the default earlier. However, whether this is the same case for incorrect trials is unclear (Fig. 4.5C).

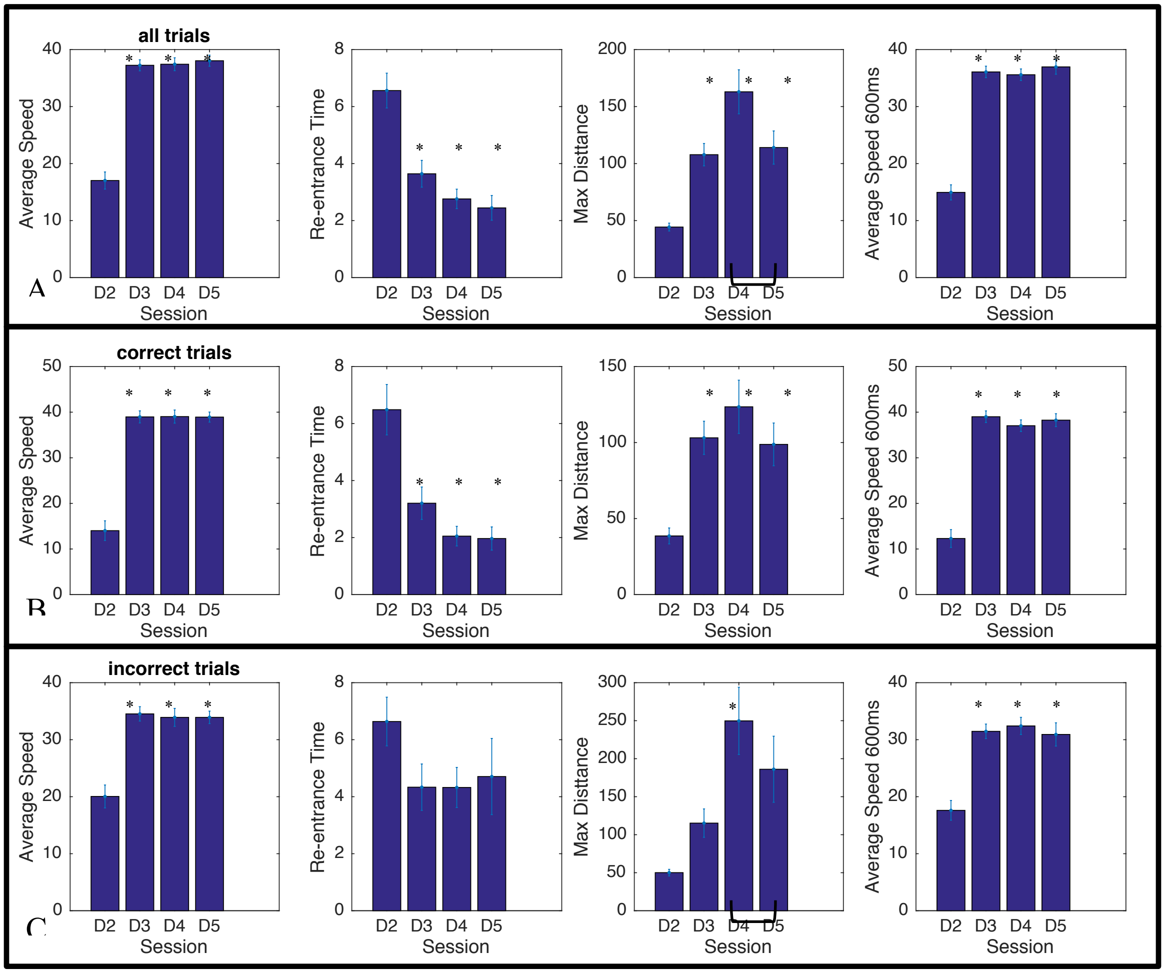

Figure 4.5. Summary of statistics for the high-dimension data: (A) Statistics with all the trials

taken into account. (B) Statistics only the correct trials account for. (C) Statistics only the incorrect trials account for. Re-entrance Time is defined as the time it takes since the onset of sound for the trajectory to return and stay in the initial baseline sphere. Average Speed is defined as the mean speed for the trajectories to re-enter the initial baseline sphere. The farthest point the trajectory reaches before re-entering the initial baseline sphere is Max Distance. Average Speed 600ms refers to the average speed of the travelling trajectory during the 600 s period (tone onset-beginning of air puff). Significance tests were performed using one-way ANOVA and corresponding post-hoc analysis. * indicates (α=0.05) statistical significance vs D2 (first day of learning). Days connected at the bottom of the graph also show statistical significance (α=0.05) against each other. The bar graph and the corresponding error bar represents mean±SEM.

Discussion

GPFA has shown very powerful capability in exploratory analysis and visualization of our data set in the low-dimension representation by optimizing the degree of smoothing and the relationship between the low-dimensional neural trajectory and the high-dimensional observed activity jointly. Such an approach allows for the attempt to determine an appropriate dynamical model that describes how the neural state evolves over time.

However, in practice, as well as literature has suggested, GPFA can be very sensitive to noise generated by low-firing neurons, and cross-talking between neurons (Yu *et al.*, 2009), which certainly is very troublesome in our data set due to the unavoidable overlapping of ROIs as projecting the 3D volume onto a 2D plane in imaging. Such defect in the data can cause serious problems, for instance, jagged output trajectories and the algorithm’s inertia to converge, and our experiment’s low sampling rate (20 Hz) certainly does not help in this case. Hence, pre-analysis cleaning is very necessary and important, e.g., removal of irresponsive and cross-talking neurons.

Plotting 1D and 2D GPFA projections offers constructive insight regarding the dynamics of the high-dimension network, but our data set has also suggested those plots are sometimes hard to interpret. Due to the low sampling rate and less-than-perfect smoothness of the trajectories, further smoothing and interpolation might be needed. In this analysis, we used local regression with weighted linear least squares and a 1st degree polynomial model to further smoothen the low-dimension neural trajectories, before using piecewise cubic spline for interpolation.

After post-GPFA processing, the evolution of the hippocampal network's dynamics was revealed. Statistics also verified similar features of high-dimensional dynamics related to learning. However, we find it hard connect such discovery with the behavior improvement of the animal. Although the correct rate of the animal behavior keeps increasing, statistical significance mostly manifests exclusively in the comparison to the first day of learning (Fig. 4.5B&C). Analyses failed to detect correlation between the network's evolution and the daily-improved behavior. On the one hand, this may be caused by the ineffectiveness in distinguishing correct and incorrect trials, which can be very sensitive to thresholding and the parameters involved. On the other hand, the hippocampal network may be involved in other internal processing which cannot be easily simplified by external trial outcome (Cunningham *et al.*, 2014).

The hippocampal network might present slightly different dynamics between correct and incorrect trials, as the statistics might indicate. When comparing the other days to the first day of learning, re-entrance time and max distance only show statistical significance in the correct trials (Fig. 4.5B&C). But we are also concerned this might be due to less number of incorrect trials available, which generates larger variance within the group as indicated in the graph with greater error bars.

Some improvement may increase the power of GPFA to make the model more suitable for our dataset. One can be to use other multidimensional smoothing techniques to substitute GP, since GPFA was originally developed to analyze electrophysiology signals, which has a much higher sampling frequency than our data. On the other hand, it may be advisable for our experiment to increase sampling rate in order to improve signal quality. It should as well be interesting to see the power of GPFA in analyzing other similar neuronal imaging data, such as genetically encoded voltage indicators like Ace FRET-opsin (St-Pierre *et al.*, 2014; Gong *et al.*, 2015).

BIBLIOGRAPHY

Badura A, Sun XR, Giovannucci A, Lynch LA, Wang SS. Fast calcium sensor proteins for monitoring neural activity. Neurophotonics. 2014 Oct;1(2):025008.

Bouchard KE, Mesgarani N, Johnson K, Chang EF. Functional organization of human sensorimotor cortex for speech articulation. Nature. 2013 Mar 21;495(7441):327–332.

Briggman KL, Abarbanel HD, Kristan WB. Optical imaging of neuronal populations during decision-making. Science. 2005 Feb 11;307(5711):896–901.

Broome BM, Jayaraman V, Laurent G. Encoding and decoding of overlapping odor sequences. Neuron. 2006 Aug 17;51(4):467–482.

Chen TW, Wardill TJ, Sun Y, Pulver SR, Renninger SL, Baohan A, Schreiter ER, Kerr RA, Orger MB, Jayaraman V, Looger LL. Ultrasensitive fluorescent proteins for imaging neuronal activity. Nature. 2013 Jul 18;499(7458):295–300.

Churchland MM, Yu BM, Cunningham JP, Sugrue LP, Cohen MR, Corrado GS, Newsome WT, Clark AM, Hosseini P, Scott BB, Bradley DC. Stimulus onset quenches neural variability: a widespread cortical phenomenon. Nature Neuroscience. 2010 Mar 1;13(3):369–378.

Churchland MM, Cunningham JP, Kaufman MT, Foster JD, Nuyujukian P, Ryu SI, Shenoy KV. Neural population dynamics during reaching. Nature. 2012 Jul 5;487(7405):51–56.

Cohen MR, Maunsell JH. A neuronal population measure of attention predicts behavioral performance on individual trials. Journal of Neuroscience. 2010 Nov 10;30(45): 15241.

Cunningham JP, Byron MY. Dimensionality reduction for large-scale neural recordings. Nature Neuroscience. 2014 Nov 1;17(11):1500–1509.

Durstewitz D, Vittoz NM, Floresco SB, Seamans JK. Abrupt transitions between prefrontal neural ensemble states accompany behavioral transitions during rule learning. Neuron. 2010 May 13;66(3):438.

Gong Y, Huang C, Li JZ, Grewe BF, Zhang Y, Eismann S, Schnitzer MJ. High-speed recording of neural spikes in awake mice and flies with a fluorescent voltage sensor. Science. 2015 Dec 11;350(6266):1361–1366.

Harvey CD, Coen P, Tank DW. Choice-specific sequences in parietal cortex during a virtual-navigation decision task. Nature. 2012 Apr 5;484(7392):62–68.

Kaufman MT, Churchland MM, Ryu SI, Shenoy KV. Cortical activity in the null space: permitting preparation without movement. Nature Neuroscience. 2014 Mar;17(3): 440.

Kihlberg JK, Herson JH, Schotz WE. Square root transformation revisited. Applied Statistics. 1972 Jan 1:76–81.

Luczak A, Barthó P, Harris KD. Spontaneous events outline the realm of possible sensory responses in neocortical populations. Neuron. 2009 May 14;62(3):413.

Machens CK, Romo R, Brody CD. Functional, But Not Anatomical, Separation of “What” and “When” in Prefrontal Cortex. Journal of Neuroscience. 2010 Jan 6;30(1):350.

Mante V, Sussillo D, Shenoy KV, Newsome WT. Context-dependent computation by recurrent dynamics in prefrontal cortex. Nature. 2013 Nov 7;503(7474):78.

Mazor O, Laurent G. Transient dynamics versus fixed points in odor representations by locust antennal lobe projection neurons. Neuron. 2005 Nov 23;48(4):661–673.

Mohammed AI, Gritton HJ, Tseng HA, Bucklin ME, Yao Z, Han X. An integrative approach for analyzing hundreds of neurons in task performing mice using wide-field calcium imaging. Scientific Reports. 2016;6.

Rigotti M, Barak O, Warden MR, Wang XJ, Daw ND, Miller EK, Fusi S. The importance of mixed selectivity in complex cognitive tasks. Nature. 2013 May 30;497(7451): 585–590.

Saha D, Leong K, Li C, Peterson S, Siegel G, Raman B. A spatiotemporal coding mechanism for background-invariant odor recognition. Nature Neuroscience. 2013 Dec;16(12):1830.

Stokes MG, Kusunoki M, Sigala N, Nili H, Gaffan D, Duncan J. Dynamic coding for cognitive control in prefrontal cortex. Neuron. 2013 Apr 24;78(2):364–375.

Storace DA, Braubach OR, Jin L, Cohen LB, Sung U. Monitoring brain activity with protein voltage and calcium sensors. Scientific Reports. 2015 May 13;5:10212.

St-Pierre F, Marshall JD, Yang Y, Gong Y, Schnitzer MJ, Lin MZ. High-fidelity optical reporting of neuronal electrical activity with an ultrafast fluorescent voltage sensor. Nature Neuroscience. 2014 Jun 1;17(6):884–889.

Sun XR, Badura A, Pacheco DA, Lynch LA, Schneider ER, Taylor MP, Hogue IB, Enquist LW, Murthy M, Wang SS. Fast GCaMPs for improved tracking of neuronal activity. Nature Communications. 2013 Jul 18;4.

Vogelstein JT, Packer AM, Machado TA, Sippy T, Babadi B, Yuste R, Paninski L. Fast nonnegative deconvolution for spike train inference from population calcium imaging. Journal of Neurophysiology. 2010 Dec 1;104(6):3691–3704.

Yu BM, Cunningham JP, Santhanam G, Ryu SI, Shenoy KV, Sahani M. Gaussian-process factor analysis for low-dimensional single-trial analysis of neural population activity. Journal of Neurophysiology. 2009 Jul;102(1):614.

CURRICULUM VITAE

Zhaojie YAO, 1990–
(585)732-3125 • zjyao@bu.edu
3720 15th Ave NE, Seattle, WA 98105

EDUCATIONAL BACKGROUND

COLLEGE OF ENGINEERING, BOSTON UNIVERSITY — **Boston, MA**
DEPARTMENT OF BIOMEDICAL ENGINEERING — *2014–present*

GPA: 3.81/4.0
Master of Science in Biomedical Engineering

CHU KOCHEN HONORS COLLEGE, ZHEJIANG UNIVERSITY — **Hangzhou, CHINA**
SCHOOL OF MEDICINE — *2009–2014*

GPA: 3.82/4.0
Bachelor of Medicine in Basic Medical Sciences
Minor in English Language and Literature

HANGZHOU FOREIGN LANGUAGE SCHOOL — **Hangzhou, CHINA**
2003–2009

RESEARCH EXPERIENCE

HAN NEUROENGINEERING LAB — **Boston, MA**
BOSTON UNIVERSITY — *2014–present*

Research Assistant supervised by Professor Xue Han

- Statistical analysis of Neurophysiology data
- Signal processing and data analysis for relationship between prefrontal and auditory cortices in tone devaluation learning in mice using electrophysiological recording
- Data analysis for development of an integrative approach for analyzing hundreds of neurons in calcium imaging
- Thesis on *Development of Analysis Approaches to Calcium-imaging Data of Hippocampal Neurons Associated with Classical Conditioning in Mice*

INSTITUTE OF NEUROSCIENCE — **Hangzhou, CHINA**
ZHEJIANG UNIVERSITY — *2011–2014*

Research Training supervised by Professor Wang XI & Professor Shumin DUAN

- Excelled in mainstream biomedical lab techniques in Neuroscience
- Bachelor thesis on *Ventrolateral Preoptic GABAergic Neuronal Activity During Light-induced Sleep in Mice*

AAB CARDIOVASCULAR RESEARCH INSTITUTE — **Rochester, NY**
UNIVERSITY OF ROCHESTER — *July 2013–August 2013*

Research Training supervised by Professor Bradford C. Berk

- Experiments concerning the projects about the effect of RpL17, PLZF, etc., in carotid artery

- Tested the lab's Bio-Rad System and its feasibility for Western Blot imaging

WOMEN'S HOSPITAL, SCHOOL OF MEDICINE **Hangzhou, CHINA**
ZHEJIANG UNIVERSITY *2011–2012*

Research Training supervised by Professor Lili HUANG

- Database development and data analysis with EpiData, Access and SPSS in the epidemiological investigation on medical abortion in Zhejiang Province
- ***Analysis on the Acceptability of Medical Abortion and its Influencing Factors***, published in *Chinese Journal of Family Planning* (2012)

PUBLICATION

- *Mohammed, A. et al.* ***'An Integrative Approach for Analyzing Hundreds of Neurons in Task Performing Mice Using Wide-Field Calcium Imaging'*** accepted by *Scientific Reports*

INTERNSHIP EXPERIENCE

THE SECOND AFFILIATED HOSPITAL, ZHEJIANG UNIVERSITY **Hangzhou, CHINA**
Department of Neurology • Department of Psychiatry *2013*

Clinical Rotation

THE FIRST AFFILIATED HOSPITAL, ZHEJIANG UNIVERSITY **Hangzhou, CHINA**
Department of Internal Medicine • Department of Surgery *2012–2013*
Department of Imaging and Radiology • Department of Infectious Diseases

Clinical Rotation

WOMEN'S HOSPITAL, ZHEJIANG UNIVERSITY **Hangzhou, CHINA**
Department of Gynecology • Department of Obstetrics *2012–2013*

Clinical Rotation

THE CHILDREN'S HOSPITAL, ZHEJIANG UNIVERSITY **Hangzhou, CHINA**
Department of Neonatology • Department of Pediatrics *2012–2013*
Department of Internal Medicine • Department of Neurology

Clinical Rotation

HONORS AND AWARDS

Graduated with **Chu Kochen Honors** **Hangzhou, CHINA**
ZHEJIANG UNIVERSITY *2014*

Scholarship for Excellent Academic Performance **Hangzhou, CHINA**
ZHEJIANG UNIVERSITY *2010–2013*

JASSO Scholarship **Tokyo, JAPAN**
TOKYO INSTITUTE OF TECHNOLOGY *2012*